Research Square

Preprints are preliminary reports that have not undergone peer review.
They should not be considered conclusive, used to inform clinical practice,
or referenced by the media as validated information.

Whole-body control of an ultra-high-aspect-ratio passive-joint aircraft

Entongh Zhu
Northwestern Polytechnical University
Zhou Zhou
Northwestern Polytechnical University
Jiachen Wang
Northwestern Polytechnical University
Yunheng Wu
Northwestern Polytechnical University
Rui Wang
wangrui@nwpu.edu.cn
Northwestern Polytechnical University

Article

Keywords: high-aspect-ratio aircraft, multibody aircraft, distributed control, morphing control, whole-body control

Posted Date: November 25th, 2026

DOI: https://doi.org/10.21203/rs.3.rs-10675343/v1

License: This work is licensed under a Creative Commons Attribution 4.0 International License.
Read Full License

Additional Declarations: No competing interests reported.

Whole-body control of an ultra-high-aspect-ratio passive-joint aircraft

Entong Zhu[1], Zhou Zhou[1*], Jiachen Wang[1], Yunheng Wu[1], Rui Wang[1*]

[1*]School of Aeronautics, Northwestern Polytechnical University, Xi'an, People's Republic of China.

*Corresponding author(s). E-mail(s): zhouzhou@nwpu.edu.cn; wangrui@nwpu.edu.cn;
Contributing authors: zhuet@mail.nwpu.edu.cn;

Abstract

High-aspect-ratio wings improve aerodynamic efficiency and are therefore preferred for long-endurance aircraft. However, these slender wings remain difficult to realize in practice because lightweight long-span structures are prone to structural instability and undergo nonlinear deformation that is difficult to observe and regulate accurately. Here we report a passive-joint modular aircraft that discretizes a continuous flexible wing into mutually movable modules connected by relaxed passive joints. This design converts continuous, nonlinear deformation into finite morphology coordinates with distributed sensing and actuation. We develop a multibody model and an equivalent-attitude overall controller that separates fast morphology stabilization from slower overall maneuvering. To recover roll authority at large span, each module also uses local pitch as a distributed aerodynamic actuator, allowing internal shape to contribute to global roll control. Flight tests show that passive-joint compliance reduces bending-strain transfer, distributed pitch actuation produces overall roll recovery, and a seven-module, 10.5 m span, aspect-ratio-51 prototype maintains stable outdoor flight. These results show that structural deformation can be stabilized and used as an indirect aerodynamic actuation mechanism, rather than only being rejected as a disturbance, providing a scalable design principle for high-aspect-ratio aircraft.

Keywords: high-aspect-ratio aircraft, multibody aircraft, distributed control, morphing control, whole-body control

1 Introduction

Long-endurance missions favor lightweight high-aspect-ratio aircraft because slender wings improve aerodynamic efficiency [1, 2]. However, the same lightweight and slender structures are inherently vulnerable: long load-transfer paths reduce stiffness and make the aircraft sensitive to turbulence-induced spanwise deformation, coupled aeroelastic flight dynamics and structural failure [1, 3, 4]. Existing solutions mainly address this problem through structural optimization, aeroelastic tailoring or active load alleviation [5–9]. These approaches primarily limit deformation within a continuous airframe, but increasing aspect ratio or span scale further introduces rapidly growing system dimensionality and structural-realization challenges.

Providing a control representation that makes large-scale deformation observable and bounded offers a route to extending the performance limits of this class of aircraft. We discretize the span into complete modules connected by relaxed passive joints with relative roll and relative twist, implemented mechanically as relative pitch between adjacent modules, to interrupt bending and torsional load-transfer paths. Each module becomes an aircraft-like body with its own sensing, propulsion and aerodynamic control surfaces, so a continuous flexible wing is converted into a finite-dimensional multibody robot. This design is related to previous wingtip-coupled, wingtip-docked and meta-aircraft concepts [10–23]. These studies established the feasibility of wingtip-linked aircraft and clarified associated flight-dynamic, controllability and flight-test challenges [11–13, 18, 21, 24]. However, existing demonstrations generally involve two, or at most a small number of, connected aircraft, constrain most internal degrees of freedom or use control strategies that keep the assembly close to a rigid-body equivalent [14, 15, 21, 25]. They have not developed a scalable control representation for coordinated multi-module motion in which released morphology is an explicit flight state and module-to-module motion conflicts are resolved during flight.

We address this gap by proposing a general distributed sensing and control framework for multi-module flight, converting continuous, nonlinear and difficult-to-measure elastic deformation into finite, controllable relative morphing states. Bending deformation is represented as relative roll and stabilized in feedback through aerodynamic surfaces, whereas torsion is not only suppressed but also exploited through distributed body actuation, with local pitch commands regulating spanwise lift to generate roll authority. An equivalent-attitude definition resolves the multi-reference-frame problem and separates fast morphology stabilization from slower overall roll control. A decoupled morphology and overall attitude controller then supports both shape stabilization and trajectory tracking. Here, *whole-body* in the title refers to a distributed sensing-and-actuation organization in which all modules participate in aircraft-level control.

First, a three-module platform shows that relaxed joints reduce the wing stress level to about 28% of that with tight joints, and the same relaxed-joint design is then scaled to a seven-module aircraft. The seven-module aircraft completes hand launch, stabilized flight, circular loitering and landing while maintaining its morphology and tracking the commanded path. These results provide a design and control route for ultra-high-aspect-ratio aircraft that is less dependent on structural approaches that are already approaching practical limits.

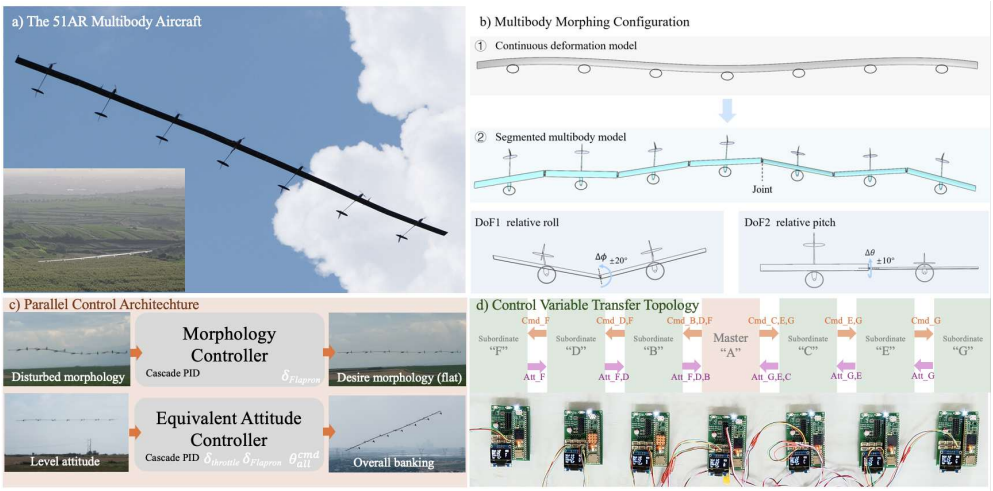


Fig. 1 Overall design and control architecture of the passive-joint modular aircraft. **a** 7-module snapshot in air. **b** Spanwise discretization released degrees of freedom. **c** Parallel, allocation-decoupled control structure consisting of a morphology controller and an equivalent-attitude controller. **d** Information-transfer topology of the flight controllers installed on each module. The central module in geometry serves as the master module in the control architecture. The master module sends aileron, throttle and desired-pitch commands to the peripheral modules, while the peripheral modules relay attitude information back to the master module through the hierarchy.

2 Results

2.1 Distributed multibody discretization converts structural deformation into controllable morphology

We developed a whole-body-controlled modular aircraft with an aspect ratio of 51 (Fig. 1a). The design starts from an ultra-high-aspect-ratio wing that provides high aerodynamic efficiency, and discretizes the span into multiple medium-scale modules connected tip-to-tip by passive joints with limited relative-roll and relative-twist degrees of freedom (Fig. 1b). Each module carries its own inertial sensing, local controller, propulsion system, trailing-edge surfaces and tail actuator. Each module was designed and manufactured as a moderate-aspect-ratio aircraft with an aspect ratio of approximately 7.3. Connecting seven such modules produced an aspect-ratio-51 aircraft without requiring any individual module to be manufactured as an ultra-high-aspect-ratio structure. The released wing therefore becomes a finite-dimensional multi-input, multi-output robotic system rather than a flexible structure with unmeasured deformation. Relative roll and relative twist are measured explicitly and assigned as morphology states for feedback control.

Using only trailing-edge surfaces would couple relative-roll control with relative-twist control because they produce lift increments and pitching moments of comparable magnitude. Each module therefore includes a horizontal tail and an elevator located farther from the centre of mass, which primarily generates pitch-control moment.

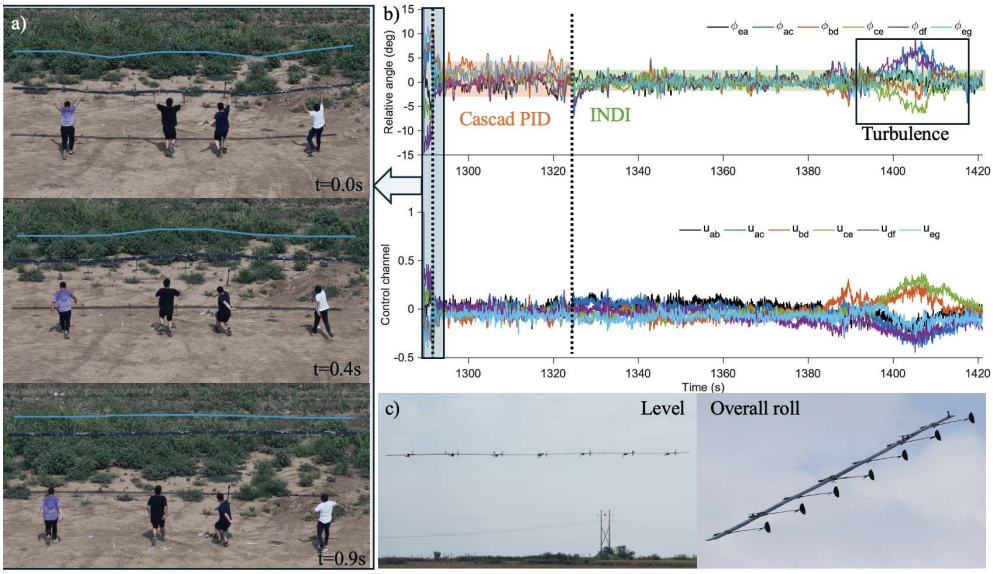


Fig. 2 Released morphology remains bounded during hand launch and sustained flight. **a** Image sequence of the hand-launch process, showing the initial morphology perturbation and recovery within approximately 1 s. **b** Relative-angle and control-channel histories during sustained flight, showing the transition from cascaded PID to INDI control and the response to turbulence. **c** Flight images showing morphology maintenance during level flight and an aircraft-level roll maneuver.

To stabilize morphology while regulating overall motion, the morphology-stabilization controller and equivalent-attitude controller run as parallel, allocation-decoupled loops (Fig. 1c). Here, parallel means that the two controllers are not arranged as inner and outer loops, and decoupled means that each controller output lies in the null space of the other controller's allocation matrix. The trailing-edge surfaces can then be used mainly for fast morphology stabilization, while the tail controls local pitch and twist.

A distributed sensing and semi-centralized flight-control architecture implements these loops on the aircraft (Fig. 1d). Local controllers estimate module attitude, angular velocity and acceleration, and transmit these states through an interconnection network to the main controller. The main controller reconstructs global morphology states and equivalent attitude, simultaneously performs morphology stabilization, whole-body control and trajectory tracking, and then distributes local pitch commands, aileron surface commands and propulsion commands back to the modules. Inter-module state exchange in this platform enters the inner-loop feedback path directly. To avoid timing conflicts caused by delayed or asynchronous control updates, we implemented the controller on a custom Teensy-based embedded platform, allowing sensing, communication, control computation and actuator updates to be scheduled as one tightly timed loop.

During hand launch, the released morphology was strongly perturbed, with several relative angles transiently reaching approximately 10–15 deg (Fig. 2). After the aircraft entered sustained flight, the configuration controller drove the measured relative deformations back toward 0 deg, showing that the passive degrees of freedom were actively stabilized rather than left as unobserved deformation. Under cascaded PID control, residual morphology oscillations remained at about 3–5 deg. After switching to INDI, most relative-angle fluctuations decreased to about 1–3 deg, indicating improved suppression of configuration perturbations while maintaining the relaxed passive-joint morphology near its commanded state. No morphology divergence was observed in these controlled flights, in contrast to the uncontrolled configuration divergence reported previously [26].

2.2 Passive joints and active control reduce structural moment transfer at large span

We tested whether passive-joint compliance could reduce structural moment transfer without leaving the wing morphology uncontrolled. On the three-module platform, we compared high- and low-stiffness passive-joint settings in repeated flights under similar wind conditions (Fig. 3c). Reducing the passive-joint stiffness from 10–15 to 1–4 $\mathrm{N\,m\,rad^{-1}}$ markedly decreased the measured bending strain. Across three flights, the mean bending-strain range decreased from 2842 to 802, corresponding to 28.2% of the high-stiffness value. The reduced joint stiffness allowed part of the structural load accommodation to appear as relative motion between modules, which was then bounded by the morphology controller through aerodynamic forces generated by the trailing-edge surfaces. We therefore adopted the low-stiffness passive-joint setting for the seven-module assembly, whose measured strain response remained close to the low-stiffness condition of the three-module platform (Fig. 3d).

2.3 Distributed pitch actuation drives overall roll maneuvers

For high-aspect-ratio flexible aircraft, overall roll control cannot be assumed to scale with conventional trailing-edge surfaces alone. As the number of connected modules increases, aileron-like inputs become less effective because the roll inertia grows faster than the available incremental roll moment. In compliant wings, the same inputs can also approach aeroelastic reversal because the intended lift increment is coupled to structural twist [27, 28]. Excessive use of trailing-edge surfaces for overall roll also consumes actuator authority that is needed to suppress internal morphology.

We therefore used distributed local pitch as an aerodynamic roll actuator. In this strategy, each module tracks a different local pitch command during a roll maneuver (Fig. 4b). The resulting spanwise angle-of-attack gradient changes the lift generated by each module and produces a overall roll moment. This mechanism uses relative twist as a controlled aerodynamic input rather than treating it only as a deformation mode to be rejected.

Flight data from the maneuver beginning at 1405 s confirmed this mechanism (Fig. 4b–d). During recovery from a right-bank attitude, the roll controller produced a positive roll-control command before allocation (Fig. 4d). Control allocation converted

this command into a spanwise local-pitch distribution, with the desired pitch increasing on one side of the span and decreasing on the other. The modules tracked these local pitch commands, producing the visible twist pattern shown in Fig. 4a. The whole aircraft then rolled back toward level flight and reached a peak roll rate of approximately 20 deg s^{-1} (Fig. 4c). These results show that local module pitch is not merely an internal morphology variable, but an aerodynamic control input that converts module-level pitch actuation into overall roll motion.

3 Discussion

Rather than addressing deformation in high-aspect-ratio aircraft only through structural stiffening or gust alleviation, the work introduces a whole-body control approach. In this representation, deformation is not treated only as an infinite-dimensional and difficult-to-observe disturbance to be suppressed, but as a measurable, controllable and partially exploitable morphology state.

Spanwise discretization makes morphology observable and controllable, while the decoupled control architecture with equivalent-attitude representation satisfies both morphology regulation and overall attitude control. Using distributed local module motion as an indirect aerodynamic actuation mechanism suppresses local twist divergence and improves roll-control authority.

The resulting control system is independent of both the specific aircraft geometry and the number of connected modules, allowing the same representation to scale to larger connected-wing systems. This distinction is important for scalability. The demonstrated aspect ratio did not rely on fabricating each module as an ultra-slender wing. Instead, seven moderate-aspect-ratio modules were composed into an aspect-ratio-51 aircraft, while passive joints interrupted long load-transfer paths and feedback control regulated the released morphology. Thus, the structural-safety and control-authority problems that usually emerge at large span were addressed at the system-architecture level.

The present implementation also defines the main boundaries of the approach. The aerodynamic model of each module is intentionally not a high-fidelity description of all local aerodynamic interactions. Instead, modelling errors are rejected by feedback, which is appropriate for stabilizing the demonstrated platform but limits purely model-based prediction outside the tested envelope. The system also places high demands on flight-controller reliability, because the current architecture does not tolerate the failure of an individual module controller. Future implementations will therefore need fault-tolerant communication, controller reconfiguration and explicit actuator-failure handling before the same approach can be used in harsher operational environments.

Overall, this work provides a scalable route for discretizing ultra-high-aspect-ratio aircraft into controllable modules, and for coordinating multiple aircraft-like bodies through a unified morphology and whole-body control representation. This perspective may be useful for scalable solar aircraft, connected-wing aircraft and modular aircraft systems.

4 Methods

4.1 Multibody dynamics model

We modelled the aircraft as a multi-rigid-body system. The dynamics follows the quasi-coordinate formulation of the Lagrange equations for multibody systems [29] and its application to compound flexible multibody aircraft [30]. The central module was chosen as the reference module and denoted A. Modules B, D and F form the left branch from the reference module, whereas modules C, E and G form the right branch, as shown in Fig. 5.

The generalized velocity and displacement vectors are

$$\begin{aligned}\mathbf{w} =&[u_a, v_a, w_a, p_a, q_a, r_a, p_{ab}, p_{ac}, p_{bd}, p_{ce}, p_{df}, p_{eg},\\ &q_{ab}, q_{ac}, q_{bd}, q_{ce}, q_{df}, q_{eg}]^T,\end{aligned} \tag{1}$$

$$\begin{aligned}\mathbf{q} =&[x_a, y_a, z_a, \phi_a, \theta_a, \psi_a, \phi_{ab}, \phi_{ac}, \phi_{bd}, \phi_{ce}, \phi_{df}, \phi_{eg},\\ &\theta_{ab}, \theta_{ac}, \theta_{bd}, \theta_{ce}, \theta_{df}, \theta_{eg}]^T.\end{aligned} \tag{2}$$

Here u_a, v_a, w_a and p_a, q_a, r_a are the translational and angular velocities of the reference module. The variables ϕ_a, θ_a, ψ_a are its Euler angles. The variables ϕ_{ij}, θ_{ij}, p_{ij} and q_{ij} describe the relative roll, relative twist and their rates between adjacent modules i and j. The positive directions of relative roll are defined by the arrows in Fig. 5. ϕ_{ab}, ϕ_{ac}, ϕ_{df} and ϕ_{eg} are positive in the illustrated directions, whereas ϕ_{bd} and ϕ_{ce} are negative under the same convention.

The multibody dynamics are written as

$$\frac{d}{dt}\frac{\partial L}{\partial \mathbf{w}} + \mathbf{H}\frac{\partial L}{\partial \mathbf{w}} - \mathbf{J}^T\frac{\partial L}{\partial \mathbf{q}} = \mathbf{Q}^*, \tag{3}$$

with

$$L = \sum_{i=1}^{n} T_i - \sum_{i=1}^{n} V_i, \tag{4}$$

Here T_i and V_i are the kinetic and potential energies of the ith body. $\mathbf{H}$ describes the quasi-coordinate velocity coupling, and $\mathbf{J}$ maps generalized-coordinate rates to body-axis velocities. $\mathbf{Q}^*$ contains the generalized forces and moments from aerodynamics, propulsion, gravity and passive-joint effects. Equivalently, the equations can be expressed in state-space form as

$$\dot{\mathbf{w}} = \mathbf{M}^{-1}\left(\mathbf{Q}^* - \dot{\mathbf{M}}\mathbf{w} - \mathbf{H}\mathbf{M}\mathbf{w} + \mathbf{J}^T\frac{\partial L}{\partial \mathbf{q}}\right). \tag{5}$$

The generalized mass matrix $\mathbf{M}$ is assembled from the inertia tensor of each module through the serial parallel-axis relation. The aerodynamic forces of each module are computed in its local frame and assembled into $\mathbf{Q}^*$ through the same topology relation.

4.2 Equivalent attitude definition

The relaxed joints make the attitude of any single module insufficient as an overall attitude reference. Any single-module attitude contains both the overall roll tendency and local morphology motion. Using it directly would feed local configuration oscillations into the controlled overall attitude variable. Following the resultant aerodynamic force principle, we established the equivalent-attitude definition for the seven-module system, as shown in Fig. 6a. This construction represents the aircraft-level motion tendency and separates lower-frequency overall roll motion from higher-frequency relative-shape perturbations. As shown in Fig. 6b, the equivalent roll angle follows the same overall trend as the reference-module roll angle, but its spectral content is more concentrated at low frequency without adding an extra low-pass filter to the attitude definition. The separation is most evident over 0.7–3.0 Hz (Fig. 6c). The definition is based on the lateral component of the distributed lift,

$$\sum_{i\in\mathcal{U}} L_i \sin\phi_i = \sin\phi_{\text{eq}} \sum_{i\in\mathcal{U}} L_i, \quad \mathcal{U} = \{a, b, c, d, e, f, g\}, \tag{6}$$

where L_i is the lift generated by module i. Thus, a zero equivalent roll angle corresponds to a zero resultant lateral lift component even when individual modules have non-zero local roll angles. For the seven-module robot, the equivalent roll angle is written as

$$\phi_{\text{eq}} = \arctan\left(\frac{\sum_{i\in\mathcal{U}} L_i \sin\phi_i}{\sum_{i\in\mathcal{U}} L_i \cos\phi_i}\right), \tag{7}$$

where ϕ_i is the roll angle of module i. For identical modules operating near the same trimmed lift, this expression reduces to the unweighted average direction used in the previous three-body formulation. The pitch and yaw of the equivalent body are inherited from the reference module,

$$\begin{bmatrix}\theta_{\text{eq}} & \psi_{\text{eq}}\end{bmatrix}^T = \begin{bmatrix}\theta_a & \psi_a\end{bmatrix}^T. \tag{8}$$

The relative roll between the equivalent body and the reference module is

$$\phi_{\text{relative}} = \phi_{\text{eq}} - \phi_a. \tag{9}$$

The corresponding equivalent angular velocity is expressed in the equivalent-body frame as

$$\boldsymbol{\omega}^m_{\text{eq}} = \begin{bmatrix}p_{\text{eq}} & q_{\text{eq}} & r_{\text{eq}}\end{bmatrix}^T = \mathbf{E}^{\text{eq}}_a \begin{bmatrix}0 & q_a & r_a\end{bmatrix}^T + \begin{bmatrix}\dot{\phi}_{\text{eq}} & 0 & 0\end{bmatrix}^T, \tag{10}$$

where

$$\mathbf{E}^{\text{eq}}_a = \begin{bmatrix}1 & 0 & 0\\ 0 & \cos\phi_{\text{relative}} & \sin\phi_{\text{relative}}\\ 0 & -\sin\phi_{\text{relative}} & \cos\phi_{\text{relative}}\end{bmatrix}. \tag{11}$$

Here q_a and r_a are the pitch and yaw angular velocities of the reference module, and $\dot{\phi}_{\text{eq}}$ can be approximated by the mean roll rate of the modules. This definition provides the attitude and angular-rate variables used by the overall controller while leaving the relative roll and twist coordinates available for morphology stabilization.

4.3 Decoupled control architecture

Both the morphology and the overall attitude of the multibody aircraft must be controlled. Unlike inner-loop designs that regulate the multibody aircraft as a single augmented plant [20], our controller uses two parallel loops. These loops consist of a trajectory–equivalent-attitude loop and a morphology loop (Fig. 7a). The outer-loop trajectory controller uses standard TECS and L1 guidance modules to generate the desired equivalent pitch θ^c_{eq}, desired equivalent roll ϕ^c_{eq} and throttle command. The state-reconstruction block estimates the measured equivalent attitude and angular rates ϕ^m_{eq}, θ^m_{eq}, p^m_{eq} and r^m_{eq}. It also estimates the relative morphology states ϕ^m_{ij}, p^m_{ij} and $\dot{p}^m_{ij}$.

The overall attitude controller follows the cascaded PI algorithm. For the roll channel,

$$\dot{p}^c_{\text{eq}} = k_{rp,1}\left[\frac{1}{T_{c,1}}\left(\phi^c_{\text{eq}} - \phi^m_{\text{eq}}\right) + k_{i,1}\int\left(\phi^c_{\text{eq}} - \phi^m_{\text{eq}}\right)dt - p^m_{\text{eq}}\right], \tag{12}$$

where k_{rp}, T_c and k_i are the rate-loop proportional gain, angle-loop time constant and rate-loop integral gain, respectively. The equivalent baseline allocation maps the desired equivalent angular acceleration to module-level lift increments and then to local angle-of-attack commands:

$$\Delta\mathbf{L} = \left(\mathbf{B}^{\text{att},L}_{\text{eq}}\right)^{-1}\dot{p}^{\text{cmd}}_{\text{eq}}, \tag{13}$$

$$\mathbf{B}^{\text{att},L}_{\text{eq}} = \frac{\partial\dot{\mathbf{w}}_{\text{eq}}}{\partial\dot{\mathbf{w}}}\cdot\frac{\mathbf{M}^{-1}\partial\mathbf{Q}^*}{\partial\Delta L_i} \tag{14}$$

$$\Delta\alpha_{i,\text{cmd}} = \frac{\Delta L_i}{P_i\cdot S\cdot a_i} \tag{15}$$

where $\Delta\mathbf{L}$ is the vector of allocated lift increments, P_i is the dynamic pressure at module i, S is the wing area of one module, and a_i is the local lift-curve slope.

After low-pass filtering the desired angle-of-attack increment command at 5 Hz, the increment was approximated as the desired pitch increment, $\Delta\alpha_{i,\text{cmd}} \approx \Delta\theta^c_i$. Each module therefore receives

$$\boldsymbol{\theta}^c_{B-G} = \theta^c_{\text{eq}} + \Delta\boldsymbol{\theta}^c_{B-G}, \quad \theta^c_a = \theta^c_{\text{eq}} \tag{16}$$

where $\Delta\boldsymbol{\theta}^c_{B-G}$ is the vector of allocated local pitch increments. Each module then tracks its own θ^c_i with an INDI local pitch controller, which outputs the elevator commands $\boldsymbol{\delta}^{\text{ele}}_{A-G}$. For module i, the pitch-angle error is

$$\theta^{\text{err}}_i = \theta^{\text{cmd}}_i - \theta^{mea}_i. \tag{17}$$

The boundary-function outer loop converts this error into a pitch-rate command,

$$q_c = \frac{K_e \theta_i^{\mathrm{err}}}{b^2 - \left(\theta_i^{\mathrm{err}}\right)^2} + \dot{\alpha}^{\mathrm{cmd}}. \tag{18}$$

The INDI inner loop then maps pitch-rate error to a commanded pitch acceleration and virtual input,

$$\dot{q}_c = K_w \left(q_c - q_m\right), \tag{19}$$

$$v_c = \dot{q}_c - \dot{q}_m. \tag{20}$$

The elevator command is updated incrementally as

$$\delta_{\mathrm{ele},i}^{\mathrm{cmd}} = \delta_{\mathrm{ele},i}^{0} + \frac{P_i S C_{m\delta_e}}{I_{yy}} v_c, \tag{21}$$

where θ_i^0, q_m, $\dot{q}_m$ and $\delta_{\mathrm{ele},i}^0$ are the measured pitch angle, pitch rate, pitch acceleration and previous elevator command, respectively. The effectiveness of the roll channel therefore depends on the pitch-control effectiveness of the individual modules. Equivalent-roll error generates a roll-channel command, which the baseline allocator converts into desired lift increments. These lift increments become local pitch increments and are realized by the local pitch INDI loops through the elevators.

The morphology controller uses structurally identical INDI loops for the released relative roll coordinates. For each relative coordinate, the boundary-function outer loop maps the morphology error to a commanded relative angular rate,

$$\boldsymbol{\omega}_{\mathrm{mor}}^{c} = K_e \frac{\mathbf{e}_{\mathrm{mor}}}{\mathbf{b}^2 - \mathbf{e}_{\mathrm{mor}}^2}, \tag{22}$$

Here $\mathbf{e}_{\mathrm{mor}} = \boldsymbol{\phi}_{ij}^{c,f} - \boldsymbol{\phi}_{ij}^{m}$. K_e and $\mathbf{b}$ are tuned constants, and $\boldsymbol{\phi}_{ij}^{c,f}$ is the filtered morphology command. The morphing INDI controller then computes the desired incremental virtual input,

$$\Delta\dot{\boldsymbol{\omega}}_{\mathrm{mor}}^{c} = \dot{\boldsymbol{\omega}}_{\mathrm{mor}}^{c} - \dot{\boldsymbol{\omega}}_{\mathrm{mor}}^{m}, \quad \dot{\boldsymbol{\omega}}_{\mathrm{mor}}^{c} = K_\omega \left(\boldsymbol{\omega}_{\mathrm{mor}}^{c} - \boldsymbol{\omega}_{\mathrm{mor}}^{m}\right). \tag{23}$$

The morphology-control allocation maps this virtual input to the trailing-edge surfaces through the configuration-dependent effectiveness matrix,

$$\boldsymbol{\delta}_{A-G}^{\mathrm{ail}} = \mathbf{B}_{\mathrm{mor}}^{\dagger} \Delta\dot{\boldsymbol{\omega}}_{\mathrm{mor}}^{c}, \tag{24}$$

where $\mathbf{B}_{\mathrm{mor}}$ maps trailing-edge surface deflections to relative-roll generalized accelerations, and $(\cdot)^\dagger$ denotes the pseudoinverse used for allocation. All morphology commands are computed by the central controller and sent directly to the modules.

During flight tests, the aircraft first flew in stabilized mode, where remote-control inputs were interpreted as desired equivalent roll and pitch angles. It was then switched to automatic altitude-hold circular flight with a prescribed diameter of 125 m and a cruising speed of 10–12 m s^{-1} (Fig. 7b). The corresponding turn radius was about six

times the 10.5 m wingspan, representing a demanding maneuver for a high-aspect-ratio aircraft. During this maneuver, the equivalent roll and pitch angles tracked their commands with root-mean-square errors of 2.828 deg and 1.774 deg, respectively (Fig. 7c).

4.4 Flight prototype setup

The seven-module prototype was not mass-uniform. Each module had an aspect ratio of approximately 7.3. The assembled aircraft comprised seven modules, giving a total wingspan of 10.5 m and a combined aspect ratio of 51. The peripheral modules carried angle-of-attack and strain sensors and a camera, whereas the central module carried the GPS, radio telemetry and current sensor. As a result, the module masses ranged from 642 to 920 g (Fig. 8a), which introduced an additional disturbance for morphology stabilization.

The passive joints were implemented with a simplified elastic hinge to reduce drag and structural mass at the wingtip connection (Fig. 8b). Black strips bonded to the upper and lower wing surfaces provided the elastic restoring effect. Soft foam placed between adjacent modules provided compression clearance during relative motion. A thicker foam layer increased the effective deforming length of the plastic strips, thereby reducing hinge stiffness. In the top view, the plastic strips were aligned with the centre-of-gravity line of the modules, leaving the joint free to accommodate relative twist.

The flight controller of each module consisted of a Teensy 4.1 MCU, a BMI088 IMU, an LED display, servo-output pins, three serial ports for inter-module communication and three ADC ports for measuring the actual servo positions (Fig. 8c). Local attitude was estimated using a Madgwick filter. The flight controllers exchanged state and command data through a 1 Mbaud serial network and ran the control loop at 400 Hz.

Data Availability

We provide videos containing 2 views, the corresponding flight data for each experiment and the code used to produce the findings of this study.

Acknowledgements

We thank Kangdian Tao and Haoyang Wu for their help in building and repairing the aspect-ratio-51 prototype. We thank Chuandong Zhu and An Guo for help with outdoor experiments and video recording. We also thank Yuewen Ma and Xuan Wu for insights on structural dynamics.

Author Contributions

ET. Z conceived the idea and experimental design. ET. Z and R.W designed and implemented the control architecture. ET. Z, JC.W and YH.W designed and conducted the experiments. YH.W conducted the data analysis. Z.Z and R.W directed, supervised and revised the research. All authors reviewed the manuscript.

Competing Interests

The authors declare no competing interests.

References

[1] Patil, M.J., Hodges, D.H., Cesnik, C.E.S.: Nonlinear aeroelasticity and flight dynamics of high-altitude long-endurance aircraft. Journal of Aircraft **38**(1), 88–94 (2001) https://doi.org/10.2514/2.2738

[2] Su, W., Cesnik, C.E.S.: Nonlinear aeroelastic simulations of a very flexible unmanned aerial vehicle. In: 51st AIAA/ASME/ASCE/AHS/ASC Structures, Structural Dynamics, and Materials Conference (2010). https://doi.org/10.2514/6.2010-2715

[3] Noll, T.E., Brown, J.M., Perez-Davis, M.E., Ishmael, S.D., Tiffany, G.C., Gaier, M.: Investigation of the helios prototype aircraft mishap, volume i: Mishap report. Technical report, NASA (January 2004). https://www.nasa.gov/news-release/nasa-dryden-flight-research-center-news-room-news-releases-nasa-releases-helios-prototype-aircraft-mis

[4] Del Frate, J.H., Cosentino, G.B., Davis, J.G., Kidd, R.T., Hill, J.R., Wang, J.T., Shih, P., Kroo, I.M., Wang, B.P.: Technical findings, lessons learned, and recommendations resulting from the helios prototype vehicle mishap. In: NATO/RTO AVT-145 Workshop on Design Concepts, Processes and Criteria for UAV Structural Integrity (2007). https://ntrs.nasa.gov/citations/20070022260

[5] Sinha, K., Klimmek, T., Schulze, M., Handojo, V.: Loads analysis and structural optimization of a high aspect ratio, composite wing aircraft. CEAS Aeronautical Journal **12**, 233–243 (2021) https://doi.org/10.1007/s13272-021-00494-x

[6] Othman, M.F., Silva, G.H.C., Cabral, P.H., Prado, A.P., Pirrera, A., Cooper, J.E.: A robust and reliability-based aeroelastic tailoring framework for composite aircraft wings. Composite Structures **208**, 101–113 (2019) https://doi.org/10.1016/j.compstruct.2018.09.086

[7] Rajpal, D., Mitrotta, F.M.A., Socci, C.A., Sodja, J., Kassapoglou, C., De Breuker, R.: Design and testing of aeroelastically tailored composite wing under fatigue and gust loading including effect of fatigue on aeroelastic performance. Composite Structures **275**, 114373 (2021) https://doi.org/10.1016/j.compstruct.2021.114373

[8] Binder, S., Wildschek, A., De Breuker, R.: The interaction between active aeroelastic control and structural tailoring in aeroservoelastic wing design. Aerospace Science and Technology **110**, 106516 (2021) https://doi.org/10.1016/j.ast.2021.106516

[9] Senger Franco, R.A., Seibel, B., Falkena, W., Vörsmann, P.: Longitudinal load alleviation control and modeling of a high-aspect ratio wing flexible aircraft. In: Proceedings of the 8th CEAS Specialist Conference on Guidance, Navigation and Control (2026). https://doi.org/10.82124/CEAS-GNC-2026-099

[10] Anderson, C.: Dangerous experiments: Wingtip coupling at 15,000 feet. Flight Journal **5**(6), 64 (2000)

[11] Montalvo, C., Costello, M.: Meta aircraft connection dynamics. In: AIAA Guidance, Navigation, and Control Conference, p. 4677 (2012)

[12] Montalvo, C., Costello, M.: Meta aircraft flight dynamics. Journal of Aircraft **52**(1), 107–115 (2015)

[13] Troub, B., Montalvo, C.J.: Meta aircraft controllability. In: AIAA Atmospheric Flight Mechanics Conference, p. 3395 (2016)

[14] Carithers, C., Montalvo, C.: Experimental control of two connected fixed wing aircraft. Aerospace **5**(4), 113 (2018)

[15] Cobar, M., Montalvo, C.: Takeoff and landing of a wing-tip-connected meta aircraft with feedback control. Journal of Aircraft **58**(4), 733–742 (2021)

[16] Cooper, J.R., Rothhaar, P.M.: Dynamics and control of in-flight wing tip docking. Journal of Guidance, Control, and Dynamics **41**(11), 2327–2337 (2018)

[17] Köthe, A., Luckner, R.: Flight path control for a multi-body hale aircraft. In: 4th CEAS Specialist Conference on Guidance, Navigation and Control, pp. 421–442. Springer, ??? (2017)

[18] Köthe, A.: Flight mechanics and flight control for a multibody aircraft. PhD thesis, Technische Universitaet Berlin, Berlin, Germany (2019)

[19] Köthe, A., Luckner, R.: Outer-loop control law design with control allocation for a multibody aircraft. In: Proceedings of the 2019 CEAS EuroGNC Conference, Milan, Italy (2019)

[20] Köthe, A., Luckner, R.: Applying eigenstructure assignment to inner-loop flight control laws for a multibody aircraft. CEAS Aeronautical Journal **13**(1), 33–43 (2022)

[21] Yang, M., Chao, A.N., Xie, C., Yang, C.: Conceptual design and flight test of two wingtip-docked multi-body aircraft. Chinese Journal of Aeronautics **35**(12), 144–155 (2022)

[22] Chao, A., Xie, C., Yang, M., Yang, C.: Flight mechanical analysis and test of unmanned multi-body aircraft. In: International Forum on Aeroelasticity and Structural Dynamics, pp. 1–13 (2019)

[23] Zhou, W., Ma, P., Guo, Z., Wang, D., Zhou, R.: Research on wingtip-chained fixed-wing uav. Acta Aeronautica et Astronautica Sinica **43**(9), 606–622 (2022)

[24] Köthe, A., Behrens, A., Hamann, A., Nagel, P., Nowka, D., Luckner, R.: Closed-loop flight tests with an unmanned experimental multi-body aircraft. In: 17th International Forum on Aeroelasticity and Structural Dynamics, Como, Italy, pp. 1–15 (2017)

[25] Qi, P., Li, Q., Wang, Y.: Trim analysis and structured h-infinity control of wing-docked multibody aircraft. Journal of Guidance, Control, and Dynamics **47**(5), 964–978 (2024) https://doi.org/10.2514/1.G007835

[26] Zhu, E., Zhou, Z., Li, H.: Modal analysis and flight validation of compound multi-body aircraft. Aerospace **10**(5), 442 (2023) https://doi.org/10.3390/aerospace10050442

[27] Bisplinghoff, R.L., Ashley, H., Halfman, R.L.: Aeroelasticity. Addison-Wesley, ??? (1955)

[28] Wright, J.R., Cooper, J.E.: Introduction to Aircraft Aeroelasticity and Loads, 2nd edn. Wiley, ??? (2015)

[29] Meirovitch, L., Stemple, T.: Hybrid equations of motion for flexible multibody systems using quasicoordinates. Journal of Guidance, Control, and Dynamics **18**(4), 678–688 (1995) https://doi.org/10.2514/3.21447

[30] Zhu, E., Zhou, Z., Wang, G.: Aerodynamics-driven morphing control and flight test for compound flexible multibody aircraft. Journal of Guidance, Control, and Dynamics (2024) https://doi.org/10.2514/1.G008194

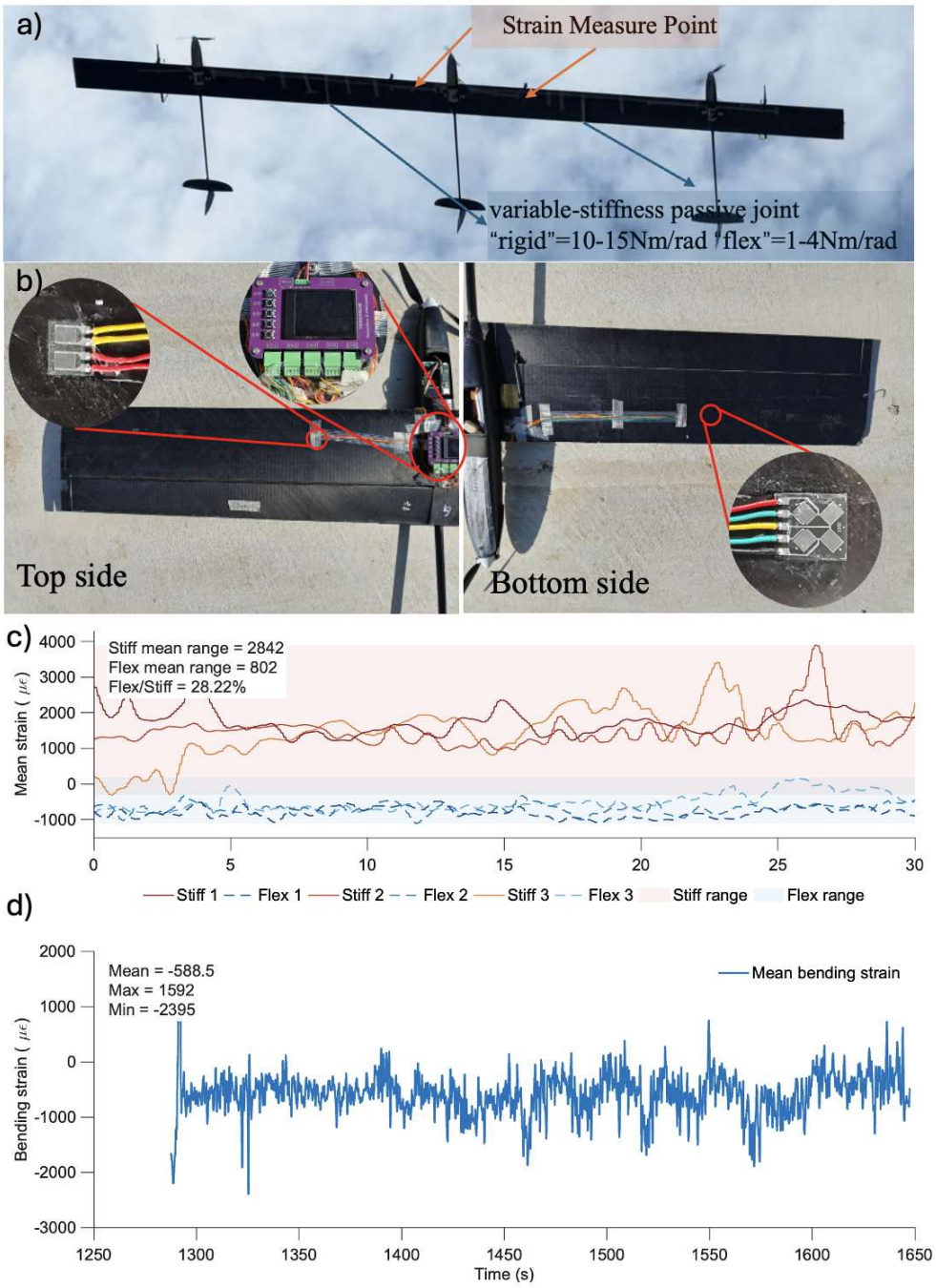


Fig. 3 Passive-joint compliance reduces bending-strain transfer in modular high-aspect-ratio flight. **a** Three-module testbed aircraft. **b** Full-bridge strain-gauge installation, with measurement points placed symmetrically on both sides of the middle module at 45% and 55% of the full span. **c** Flight-load strain under high- and low-stiffness passive-joint settings. **d** Strain response of the seven-module assembly under the low-stiffness passive-joint setting.

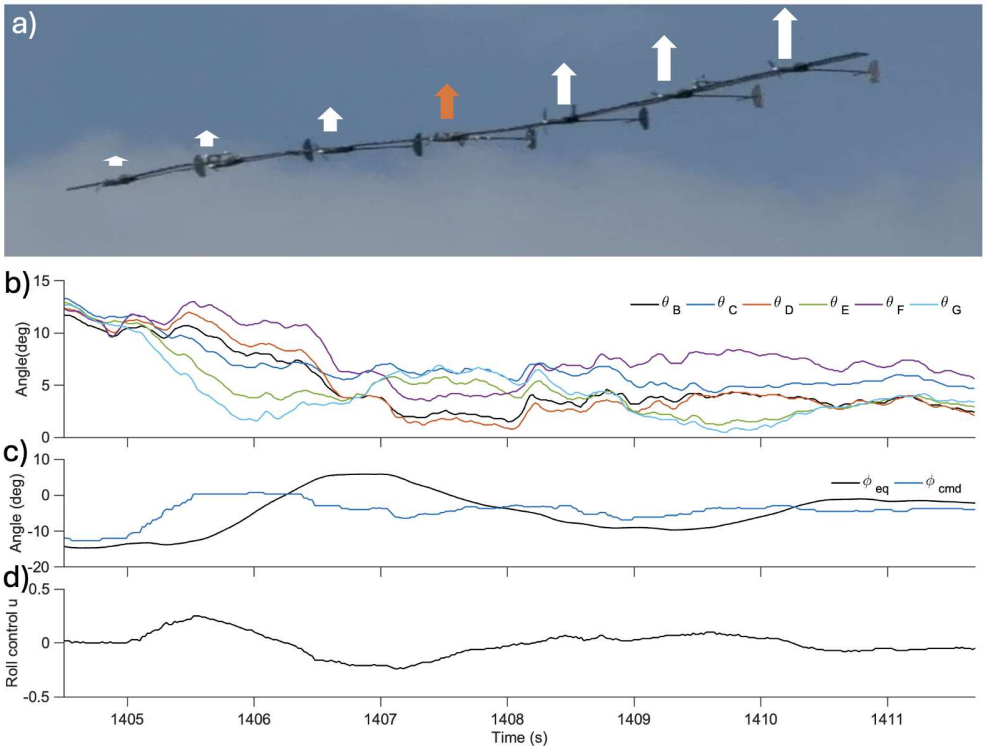


Fig. 4 Overall roll recovery generated by distributed local pitch actuation. **a** Flight image showing a spanwise pitch distribution, visible from the relative tail attitudes of the modules. Arrows indicate the instantaneous lift of the aircraft: orange arrows denote cruise lift, and white arrows denote lift during the roll maneuver. **b** Measured local pitch angles during the roll-recovery maneuver, with a maximum module-to-module pitch separation of approximately 10 deg. **c** Equivalent roll angle of the whole aircraft, showing the transient overshoot and damped recovery. **d** Roll-controller output before control allocation.

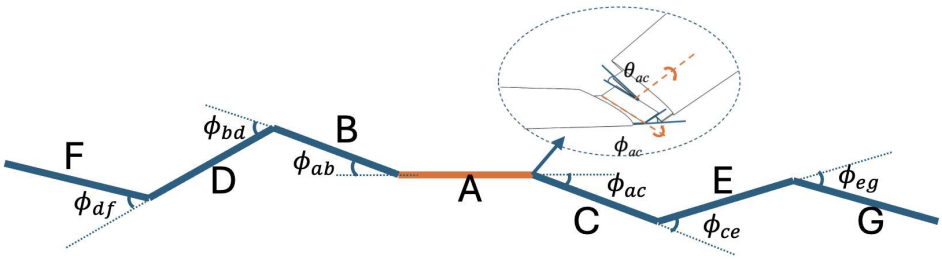


Fig. 5 Seven-module topology and relative-angle definitions used in the multibody dynamics model.

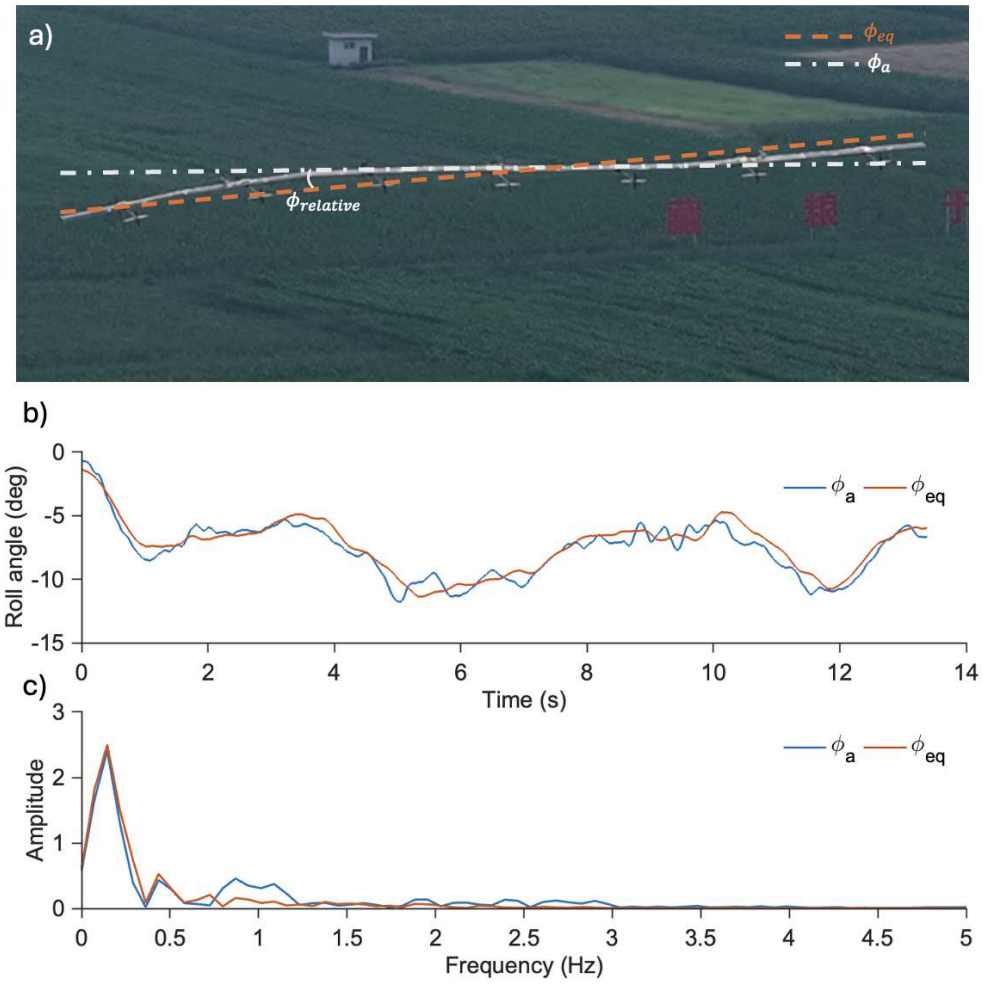


Fig. 6 Equivalent roll angle for overall attitude representation. **a** Flight snapshot illustrating the difference between the central-module roll angle, ϕ_a, and the equivalent roll angle, ϕ_{eq}. **b** Time series of the central-module roll angle and equivalent roll angle. **c** Frequency-domain comparison of the central-module roll angle and equivalent roll angle.

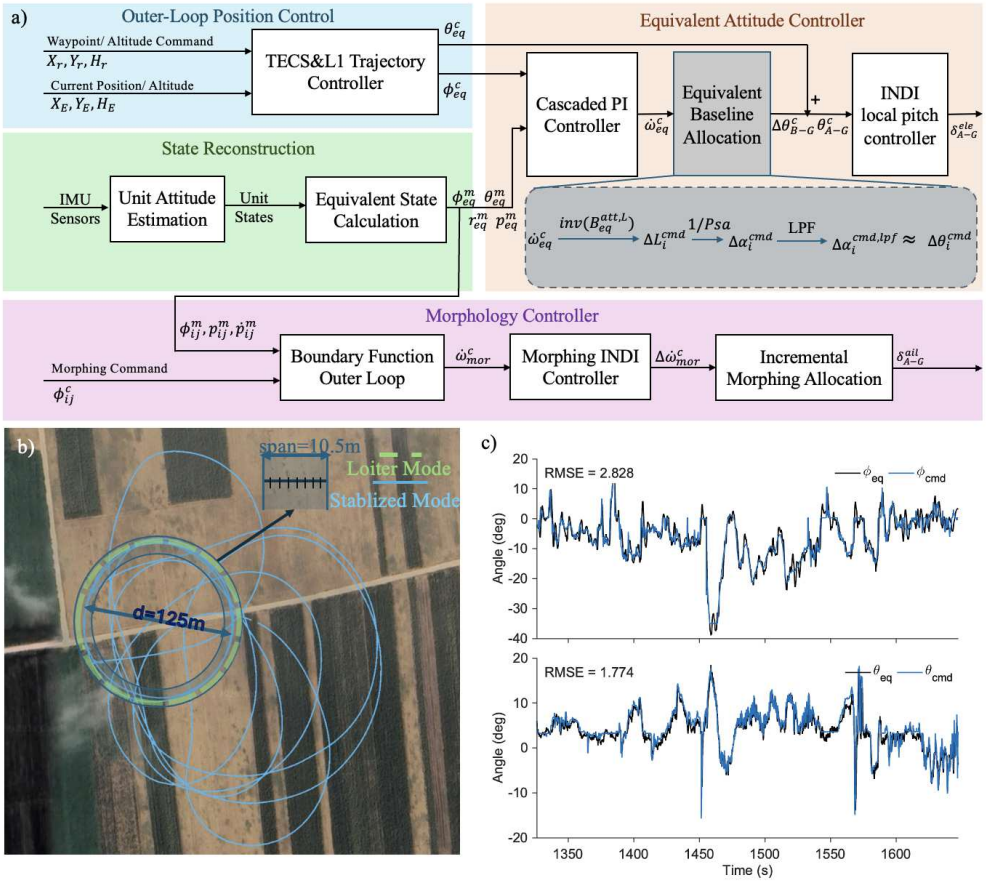


Fig. 7 Decoupled control architecture for morphology stabilization and overall maneuvering. **a** Parallel morphology and overall attitude controllers with allocation through equivalent-attitude and morphology channels. **b** Flight trajectory including stabilized mode, driven by pilot attitude inputs, and automatic loiter mode. **c** Equivalent roll and pitch command tracking during loiter flight.

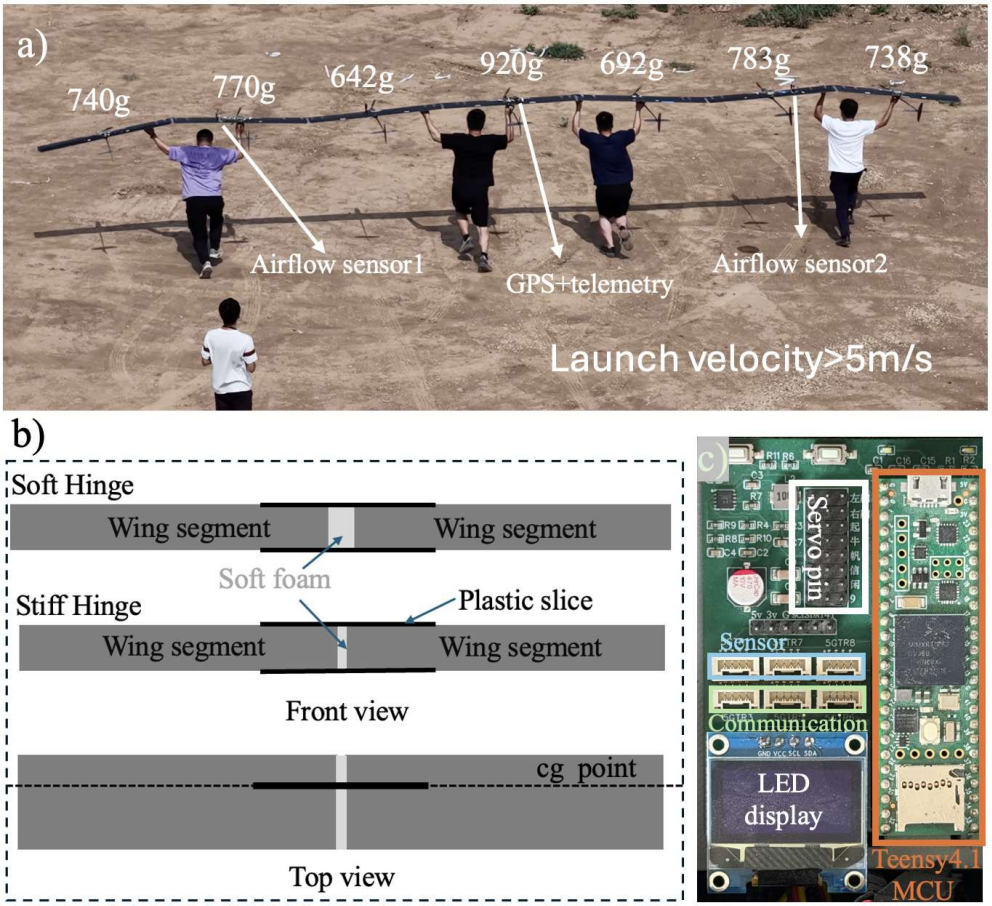


Fig. 8 Prototype setup, passive-joint implementation and custom flight-control hardware. **a** Seven-module prototype during hand launch, showing module masses and onboard sensor locations. **b** Passive-joint implementation under soft- and stiff-hinge settings. **c** Custom Teensy 4.1 flight controller with sensor, communication, servo-output and display interfaces.

Supplementary Files

This is a list of supplementary files associated with this preprint. Click to download.

- flight1.mov